nature COMMUNICATIONS

ARTICLE

Received 28 Sep 2014 | Accepted 10 Jun 2015 | Published 23 Jul 2015

DOI: 10.1038/ncomms8783

Single-photon emitting diode in silicon carbide

A. Lohrmann[1], N. Iwamoto[2], Z. Bodrog[3], S. Castelletto[4], T. Ohshima[2], T.J. Karle[1], A. Gali[3,5], S. Prawer[1], J.C. McCallum[1] & B.C. Johnson[6]

Electrically driven single-photon emitting devices have immediate applications in quantum cryptography, quantum computation and single-photon metrology. Mature device fabrication protocols and the recent observations of single defect systems with quantum functionalities make silicon carbide an ideal material to build such devices. Here, we demonstrate the fabrication of bright single-photon emitting diodes. The electrically driven emitters display fully polarized output, superior photon statistics (with a count rate of >300 kHz) and stability in both continuous and pulsed modes, all at room temperature. The atomic origin of the single-photon source is proposed. These results provide a foundation for the large scale integration of single-photon sources into a broad range of applications, such as quantum cryptography or linear optics quantum computing.

[1] School of Physics, The University of Melbourne, Victoria 3010, Australia. [2] SemiConductor Analysis and Radiation Effects Group, Japan Atomic Energy Agency, 1233 Watanuki, Takasaki, Gunma 370-1292, Japan. [3] Institute for Solid State Physics and Optics, Wigner Research Centre for Physics, Hungarian Academy of Sciences, Budapest, POB 49, H-1525, Hungary. [4] School of Aerospace, Mechanical and Manufacturing Engineering, RMIT University, Melbourne, Victoria 3001, Australia. [5] Department of Atomic Physics, Budapest University of Technology and Economics, Budafoki út 8, H-1111, Budapest, Hungary. [6] Centre for Quantum Computing and Communication Technology, School of Physics, University of Melbourne, Victoria 3010, Australia. Correspondence and requests for materials should be addressed to B.C.J. (email: johnsonb@unimelb.edu.au).

With breakthroughs in silicon carbide (SiC) growth technologies and its excellent thermal, mechanical and physical properties[1], SiC has become an outstanding wide bandgap semiconductor for both emerging optical and electronic applications. Well-developed complementary metal-oxide semiconductor (CMOS) compatible processing protocols exist for SiC providing the availability of broadband photonic optical cavities[2] and, with the possibility of controlled doping of both p- and n-type impurities[3], commercialized electronic devices. The compound nature and extensive polytypism of SiC results in a broad array of defects some of which have promising applications in quantum computing, cryptography and metrology. Optically driven single-photon emission in 4H–SiC has been demonstrated for the carbon-vacancy carbon-antisite C_vC_{Si} pair[4], the silicon vacancy (V_{Si})[5,6] and the divacancy ($V_CV_{Si}^0$)[7] and in 3C–SiC for the C_vC_{Si} pair[8]. Other single-photon emitters in wide bandgap materials such as ZnO[9] may also display similar characteristics.

To significantly enhance the practicality of single-photon emission, it is desirable to integrate single-photon emitters into a device to allow electrical pumping. Electrically driven quantum dots have been demonstrated[10–14], but these mostly operate at low temperatures. The possibility of electrical excitation at room temperature of the nitrogen vacancy defect in diamond, NV^0, has also been shown[15,16], but at present there are severe limitations on the types of devices that can be engineered with this material, namely, the inability to create a high-active n-type concentration by ion implantation.

In this work, single-photon emitters in the visible spectral range are integrated into SiC p^+n junction diodes. The fabrication of these single-photon emitting diodes is achieved by applying well-developed CMOS compatible processes including photolithography, ion implantation and annealing. Photon anti-bunching measurements indicate the quantum nature of the single defect. The emitters have high emission rates, are fully polarized and operate with high stability at room temperature, characteristics which are beneficial for quantum cryptography protocols and linear optics quantum computing[17].

Results

Single-photon source and device integration. SiC p^+n junction diodes were formed in 4H–SiC n-type epi-layers by implanting aluminium while the substrate was held at 800 °C. Results with 6H-SiC appear in Supplementary Fig. 1. To activate the dopants a post-implantation anneal of 1,600–1,800 °C was employed. During this anneal a carbon capping layer was used to prevent Si sublimation and step bunching formation[18]. No irradiation step was performed to create single defects after annealing. Fig. 1a shows the device schematic (bottom) together with the confocal microscope used to observe the material's luminescence. The dopant profile is derived from SRIM calculations which are presented in Supplementary Fig. 2. A typical current–voltage (I–V) curve from our fabricated diodes is displayed in Fig. 1b and shows the expected rectifying behaviour of a p–n junction diode with a reverse leakage current of around 1×10^{-10} A cm^{-2}. In forward bias, the device displays clear features that are dominated by the series resistance which limits the injected current. Electroluminescence (EL) is also observed when driven above the threshold voltage of $V_T \approx 3.1$ V. Further fabrication and measurement setup details are provided in the Methods section below.

The EL arises with the recombination of electrons and holes at deep-level defect states[19,20]. Fig. 1c shows an EL map of the device under an applied forward bias of 10 V. The central bright spot is a single defect with a count rate of 250 kHz and does not display any blinking behaviour. The defects are located near the SiC epilayer surface between the top aluminium contact and the floating guard rings and not in the implanted regions.

Figure 1d shows a typical EL spectrum taken at a single defect site. The spectrum displays two main components. Firstly, a

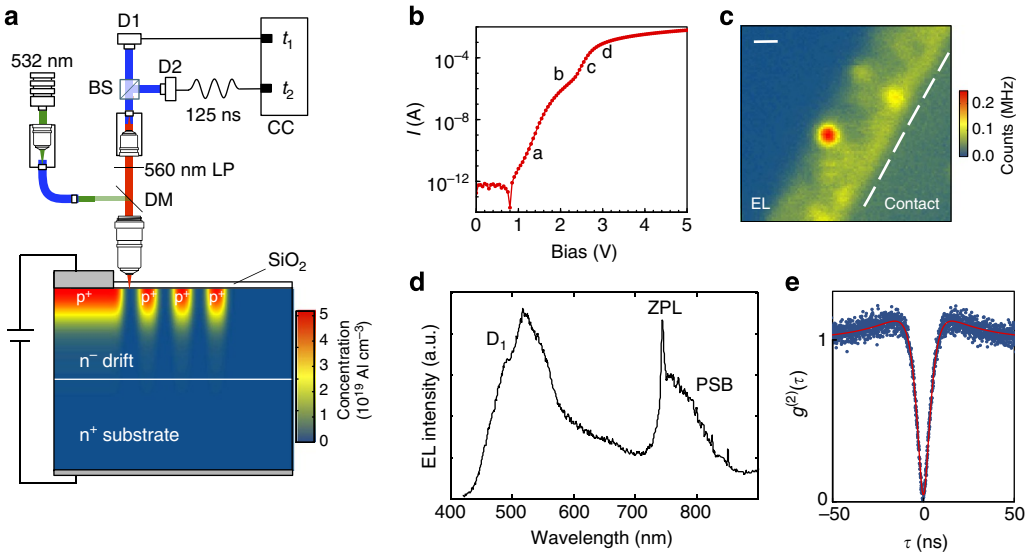

Figure 1 | Single-photon sources in fully fabricated p^+n junction diodes in 4H-SiC. (**a**) Schematic of the confocal setup used to characterize the single-photon emitters. It includes a Hanbury Brown and Twiss interferometer with two single-photon avalanche detectors (D1 and D2) connected to a correlation card (CC). The dichroic mirror (DM) was removed when in used in EL mode. A partial schematic of the device consisting of a p^+ top contact is also shown. Three floating guard rings encircle the central contact to decrease the electric field at the main contacted junction. (**b**) I–V-curve of the diode. In this device, features due to shunt resistance, tunnelling current, diffusion current and series resistance are indicated by the letters a–d, respectively. (**c**) EL map of the edge region of a device. Scale bar, 1 μm. (**d**) Room temperature EL spectrum showing the source of the background (D_1 line) and the single-photon emitter with a ZPL at 745 nm and a broad phonon side-band. (**e**) Background corrected anti-bunching traces with $g^{(2)}(\tau = 0) < 0.1$ indicating excellent single-photon emission characteristics. The detector count rates were $N_1 \approx N_2 = 160$ k.c.p.s. with $\rho = 0.82$, a total integration time of 20 min and a bin width of 64 ps.

signal arising from the D_1 centre with a weak zero-phonon line (ZPL) at 427 nm and a phonon-side band with a peak intensity around 520 nm is observed. This often appears as background luminescence in the vicinity of the implanted region and is mostly formed as a result of the implantation-induced damage, surviving the high-temperature activation anneals. The D_1 line is associated with a Si antisite (Si_C)[21,22] Secondly, in this example, ZPL emission at a wavelength of 750 nm in Fig. 1d from the diffraction limited bright spot appears. To construct the EL map of single-photon emitters shown in Fig. 1c, emission was collected through a 560 nm long-pass filter to suppress the D_1 line. Fig. 1e shows an example of the background corrected[23] anti-bunching trace with $g^{(2)}(\tau=0)<0.1$ confirming excellent single-photon emission characteristics.

While the D_1 line is relatively well known, a wide variation of ZPL positions and line shapes was observed for single defects (see Supplementary Fig. 3). To aid in the identification of these defects we studied their formation in a broad range of SiC materials with different doping densities and processing conditions. For these studies photoluminescence (PL) measurements on high-purity semi-insulating (HPSI) SiC from CREE were performed and enabled a greater number of stable defects to be studied at once. Additionally, when laser excitation was used with the single-photon emitting diodes, the single defects could not be clearly characterized as their photostability decreased and a significant background luminescence, possibly resulting from the lower quality of the highly doped layers, appeared.

The as-purchased HPSI sample showed only unstable defect emission as observed previously[4]. As mentioned above, the defects of interest in this work form and are stabilized via high-temperature annealing only. As with the EL emission described in Fig. 1, over 90% of these centres are completely photo stable. Further, it was found that if the surface roughness is allowed to degrade during a high-temperature annealing without the carbon capping layer[18], the photostability and defect density greatly decreased. The defects are thus very sensitive to the state of the surface and detailed confocal maps confirm that they exist in a narrow band close to the surface (see Supplementary Fig. 4).

A typical PL confocal map of the HPSI SiC is shown in Fig. 2a. The defect density was found to vary slightly for different samples typically in the $2-8\times10^7\,cm^{-2}$ range. Interestingly, electron irradiation of 2 MeV electrons to a fluence of $1\times10^{17}\,cm^{-2}$ did not appear to significantly increase the defect density or the type of defects observed after the high-temperature annealing.

By lowering the temperature to 80 K, most defect spectra develop sharp ZPL, with line widths ranging from 0.3 to 2 nm and could be characterized further. Fig. 2b,c show two typical single defect spectra taken at 80 K for excitation wavelengths of 532 and 633 nm, respectively. Room temperature spectra are presented in the Supplementary Fig. 3. Phonon-assisted transitions are still present as can be seen by the elevated background signal. The transverse optic and longitudinal optic phonon Raman modes are indicated. We performed spectral measurements of more than 50 defects and created a histogram of the recorded ZPL peak positions (Fig. 2d). The histogram clearly shows the variety of ZPL over the whole red spectral region. We did not observe any groups of lines as might be expected for different charge states, defects on inequivalent lattice sites or multiple defect types. Instead the lines are continuously distributed over a 200 nm range. The large spread is peculiar and will be addressed in the discussion below. In the following sections we examine several other properties shared by all observed single-photon emitters in these materials to give further scope to the discussion.

Single-photon emitter dynamics. Figure 3a,b show the background corrected anti-bunching traces of two different single defects in EL (p^+n device) and PL (HPSI sample) mode that have similar spectral characteristics, respectively. Typical signal-to-background ratios are $\rho\geq0.8$. Photon bunching around $\tau=10$ ns is evident in EL and especially in PL modes which is related to a dark metastable state. EL and PL modes differ most strikingly around $\tau=0$, where the EL anti-bunching exhibits a plateau characteristic of a double pump process[16,24]. Such a process may involve, for example, a two-step carrier capturing process. The equation that is used to fit the PL data is a double exponential, which is commonly used for three level systems[25]. A standard analysis based on such a system yields a relatively fast excited state lifetime of $t_L^{PL}=3.3\pm0.3$ ns with transitions to a dark state every 10 cycles. All other centres studied show very similar transition rates ($t_L^{PL}=2-5$ ns).

To account for the plateau that is evident in the EL data, a third exponential term is required and yields an excellent fit. Such an empirical relation has a form that may be reflective of a four-level electronic system[16,24]. Fig. 3c illustrates the $g^{(2)}(\tau=0)$ evolution under increasing injected current. Because of the faster pump rate, the $g^{(2)}(\tau=0)$ sharpens and there is a subtle increase in the photon bunching. All time constants associated with the fit increase linearly with injected current. The signal-to-background ratio did not change significantly with the injected current.

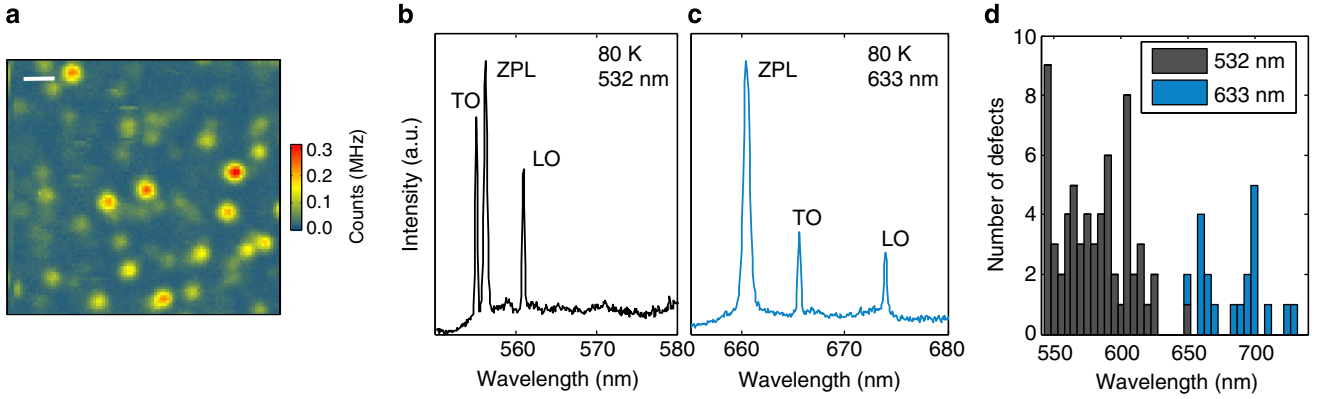

Figure 2 | Single defect PL in 4H-SiC. (**a**) Room temperature confocal map excited with 532 nm. Scale bar, 1 μm. (**b**,**c**) Single defect spectra taken at 80 K under excitation with 532 nm and 633 nm for two different defects, respectively. Transverse optic (TO) and longitudinal optic (LO) indicate Raman lines. The ZPL widths are 0.5 nm for green and 0.8 nm for red excitation. (**d**) Histogram created from more than 50 spectra indicating the number of lines per 5 nm interval.

The intensity of the single defect emission in EL varies strongly from defect-to-defect with many being well over 300 kHz. One contributing factor to the intensity variation is the distance from the p^+n junction which determines the current density at the defect location. A typical EL intensity–current curve is shown in Fig. 4a. After subtracting the linear background that originates from the D_1 centre emission (dotted line), we obtain a linear relationship. Note, that the initial non-linearity is due to the unknown current density at the defect site and does not indicate a saturating behaviour. The detector count rate reached 350 kHz at 14 mA without signs of saturation. This intensity is more than twice as bright as the saturation count rate of an optically driven single nitrogen vacancy (NV^-) in diamond investigated using the same experimental setup, and more than six times brighter than the EL saturation count rate from NV^0 defects in diamond[16]. At higher currents, some degradation in the device characteristics is observed which affects the count rate. Therefore, no true saturation behaviour has yet been observed.

In contrast, the intensity–power dependence in PL shown in Fig. 4b displays a saturation type behaviour over a count rate similar to that observed in EL but with a dependence given by, $C(P) = C_{sat}P/(P + P_{sat})$. Here, P is the excitation power, C the detector count rate, P_{sat} the saturation power and C_{sat} the saturation count rate. Fig. 4b shows a typical intensity–power curve with a saturation count rate of $C_{sat} = 0.9 \pm 0.2$ MHz and saturation power of $P_{sat} = 880 \pm 250$ μW.

Although the defect emission reaches similar count rates in both excitation modes, only the PL mode shows the beginnings of saturation behaviour. The significantly lower branching ratio in EL, indicated by the weak bunching of the $g^{(2)}(\tau)$, can therefore yield an explanation for the significantly higher count rates without saturation.

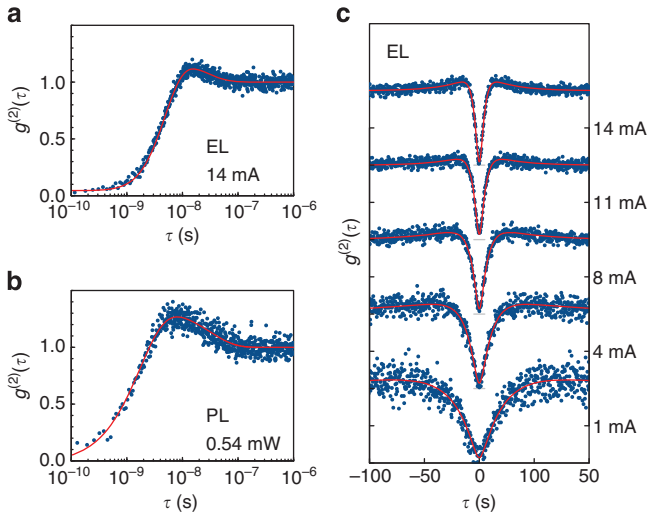

Figure 3 | Single-photon emitter dynamics. Background corrected (**a**) EL and (**b**) PL traces for two spectrally similar single-photon emitters in 4H-SiC (solid line fit described in the text). The detector count rates were 160 and 130 k.c.p.s. per detector with $\rho = 0.95$ and $\rho = 0.82$ in PL and EL, respectively. The total integration time was 400 s in PL and 20 min in EL with a bin width of 64 ps. (**c**) EL $g^{(2)}(\tau)$ traces for different currents offset vertically for clarity.

Electrically pulsed single-photon emitting diode. The single-photon emitting diodes allow the application of narrow electrical pulses for the production of near-deterministic single photons. A function generator was used to apply 20 ns voltage pulses at 10 MHz in forward bias with a peak voltage of 10 V to inject the charge carriers. A typical pulsed $g^{(2)}(\tau)$ is shown in Fig. 5a. The pulsed emission is indicated by the periodic correlation peaks. The height of the zero-order peak drops to $g^{(2)}(\tau = 0) \approx 0.2$, again unambiguously indicating single-photon emission and in fair agreement with Fig. 3. The non-zero value at $\tau = 0$ can be accounted for by the background EL from the D_1 centre arising from the implantation damage as discussed above. It should be noted that this can presumably be further reduced with the optimization of the device geometry. The count rate under these conditions was 12.2 kHz giving $\eta_{det}\eta_{col}\eta_{def} = 1.2 \times 10^{-3}$, where η_x are the detection, collection and defect photon generation efficiencies in our system, respectively. An estimation of η_{def} is determined to be $>8\%$ with $\eta_{det.} \approx 53\%$ and $\eta_{col.} \approx 3\%$. Since the device is not yet in the saturation regime (Fig. 4), this efficiency is more related to an effective recombination efficiency of the defect rather than its intrinsic quantum efficiency.

Excitation repetition rates >10 MHz decrease the count rate but this may be improved once integrated with a cavity or solid immersion lens[5] since $\eta_{col.}$ dominates the total efficiency of the system. To our knowledge, this is the first demonstration of a pulsed room temperature single-photon emitting diode.

Polarization of single centres. A λ-half wave plate and a polarizer were used to rotate and filter the single-photon emission. Fig. 5b shows the polarization behaviour for a single defect. As indicated by the dashed line, the emission intensity drops to the background level. A study of the polarization axis of more than 30 defects revealed the same fully polarized emission along three main polarization axes separated by a 60° angle (see Supplementary Fig. 5). This implies that the defect emission dipoles are oriented along the hexagonal basal plane of the SiC matrix. The same behaviour was observed in PL in absorption and emission. The close similarity of the PL and EL polarization

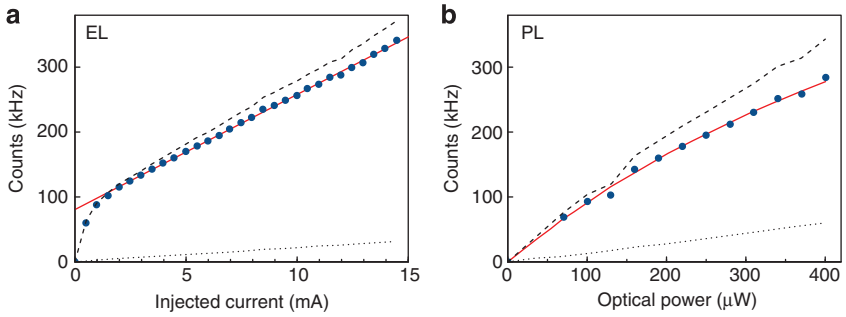

Figure 4 | Intensity-excitation power curves for single-photon emitters in 4H-SiC. Intensity curve for a single defect as a function of (**a**) current (EL) and (**b**) laser power (PL) corrected for the background (dotted line). The raw signal is indicated by the dashed line.

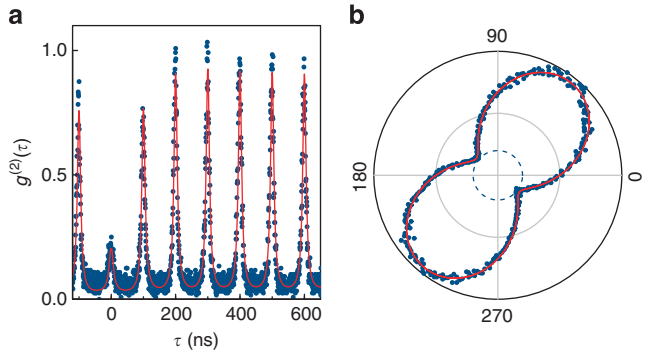

Figure 5 | Electrically pulsed excitation and polarization dependence. (**a**) Second order autocorrelation without background correction showing $g^{(2)}(\tau = 0) < 0.2$ under 10 MHz pulsed excitation where the pulse width and height were 20 ns and 10 V, respectively. (**b**) Polarization dependence of an electrically driven single emitter. The dashed circle represents the background level.

behaviour further indicates that all defects studied here have the same symmetry and therefore suggests the same origin.

Discussion

The CMOS compatibility of SiC lends unprecedented flexibility to further development of this electrically driven single-photon source. This includes further optimization of the device, its integration with optical components such as solid immersion lenses, cavities and on-chip waveguides and finally, device scale-up. Further to this, some flexibility in the integration of other defect types, such as the V_{Si} or the $C_{Si}V_C$, is also possible. For instance, defects with a lower thermal stability can be introduced at a later stage in the device processing. Optical filtering would then be needed to target specific defects.

Further optimization of the device design is expected to allow higher current densities to be generated at the defect site. This may result in single-photon count rates in the MHz regime. The count rate saturation regime (Fig. 3a) may then also be accessed to investigate the emission dynamics and quantum efficiencies in more detail. With these developments and the favourable intrinsic properties of these emitters such as their full polarization (Fig. 4b), photostability and room temperature operation, opportunities for the application of SiC to quantum information processing, quantum cryptography and single-photon metrology are foreseeable.

As mentioned above, the spectral characteristics of these sources have not previously been reported. We now discuss their possible atomic origin. Their characteristic properties are their high thermal stability, preferential formation close to the surface, wide variability in ZPL and strong polarization perpendicular to the c axis. These common characteristics suggest a common origin. Firstly, it is known that stacking faults (SFs) often form close to the surface during post-growth surface processing[26]. The variation in size and type of these SFs could explain the large ZPL variability[27]. However, the polarization of the emitted photons from SFs would be emitted parallel to the c axis because of the spatial separation of the electron and hole along the c axis in the excited state[26]. This is in contrast to the observations made here. Alternatively, the polarization and high thermal stability may be explained by a stable point defect with a high C_{3v}-symmetry. However, a single defect type residing on inequivalent sites cannot account for the observed 200 nm variance in ZPL position. We therefore conclude that the most likely origin is a combination of these two structures, namely, a thermally stable C_{3v}-symmetry point defect which is near or embedded into a SF where the luminescence of the defect involves states split from the conduction band edge as shown in Fig. 6a. Although, direct experimental evidence for such a structure is still lacking, it accounts for the spatial location of these sources, their polarization and the fact that their density cannot be enhanced by electron irradiation since the SF concentration is intrinsically low. Very few defects show a thermal stability up to 1,600 °C in 4H–SiC. One such defect is the D_1 centre (Si_C shown in Fig. 6b). In our devices, luminescence from this centre can be clearly observed (for example, Fig. 1d) and therefore certainly has high thermal stability. The D_1 centre also has a high C_{3v} symmetry with polarization perpendicular to the c axis[28]. The luminescence mechanism can be described as recombination of the electron at the split conduction band state and a localized hole on the defect site.

Ab initio calculations (see Methods) of a Si_C defect in proximity to a single cubic SF show that the ZPL energy is indeed sensitive to the defect-SF distance while also maintaining the same general recombination behaviour found for the defect in bulk 4H–SiC. Fig. 6c shows that when the defect is placed close to the SF, the ZPL energy follows the variation in the conduction band edge induced by the SF. We considered a 2.5 nm wide 3C polytype inclusion by a simplified model-Hamiltonian method (see Methods). This structure yields a triangular potential well for the conduction band electrons. We find that defects close to but above the 3C inclusion along the c axis emit light at $\sim$540 nm. Defects located inside the 3C inclusion can emit a continuous range of longer wavelength photons from the top side down to the bottom side of the inclusion. Defects beneath the 3C inclusion show emission around 750 nm. As the defect-SF distance increases, the ZPL wavelength tends to the bulk value confirmed by our *ab initio* calculations. The convergence of the ZPL wavelength to the bulk value depends on the SF-type and the immediate environment of the defect region that may contain another SF or the surface in a realistic material which can further modify the potential felt by the defect. Nevertheless, we are able to demonstrate that a variation in defect position near or inside this 3C inclusion could explain the broad variance in ZPL position and give rise to the histogram displayed in Fig. 2d.

These calculations also allowed the electronic structure and recombination kinetics at the Si_C defect to be considered in detail (Fig. 6d). The highest fully occupied defect level has an e character in the ground state which lies at $\sim$0.2 eV above the valence band edge in 4H–SiC, and no empty defect state appears in the gap. In the excited state the electron occupies an a_1 state split from the conduction band edge and leaves a hole in the strongly localized e state. This can form an optically active ^1E excited state and a lower-energy ^3E shelving state. The strong luminescence between ^1E and $^1A_1$ only produces photons with a polarization perpendicular to the c axis. Interestingly, the presence of this ^3E state could explain the photodynamics we observe in the PL. We also found that the e state in the excited state shifts down towards the valence band edge compared with the case of the ground state and has a strong interaction with the valence band-derived resonant e state. In the EL process the hole may first be captured by the valence band-derived resonant e state forming a higher-energy $^3E'$ state that can decay towards the optically active ^1E excited state by a spin–orbit interaction mediated by phonons. This may explain the four-level-like EL process described in Fig. 3. Our working model can basically account for all properties of the PL and EL single-photon sources observed in this work. Nevertheless, we do not discount other possible candidate extrinsic or intrinsic defects that have a similar electronic structure.

In conclusion, electrically driven single-photon sources operating at room temperature have been integrated into a range of

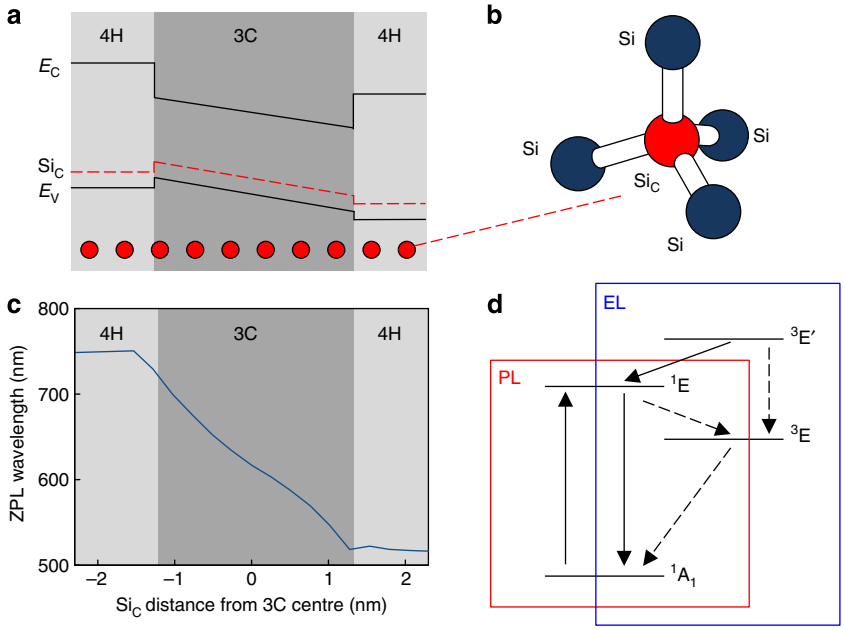

Figure 6 | Defect origin. (**a**) Schematic of the band edges of a 3C polytype inclusion in 4H–SiC[35]. The *x* axis is parallel to the *c* axis with increasing depth to the left. The location of a defect state introduced by the Si_C defect shown in (**b**) is symbolized by a red dot where the hole is strongly localized upon excitation. (**c**) The calculated ZPL wavelength as a function of the Si_C location around or inside a 2.5 nm wide 3C polytype inclusion along. (**d**) A schematic of the energy level diagram of the Si_C defect where the ground state is $^1A_1$. Fast (slow) processes are labelled by straight (dashed) arrows. PL and EL boxes indicate the states participating in the respective processes. The $^3E'$ state consists of a valence band-derived hole captured by the defect whereas the ^1E and ^3E excited states consist of a hole localized on the defect. In these excited states the electron lies on a split conduction band state thus the energies of the $^3E'$, ^1E and ^3E levels depend on the position of the conduction band edge.

SiC devices. This is achieved using CMOS compatible fabrication techniques, namely photolithography, dopant implantation and annealing. The high-temperature processing resulted in highly efficient single-photon emitters with a stable and high emission rate that exceed that of other room temperature electrically driven single-photon sources. These defect-based sources have a high thermal stability, wide variability in ZPL wavelength and a strong polarization. The recombination kinetics in EL mode showed characteristics of a double transition before radiative decay while the PL model could be characterized by a standard three level energy level scheme. A model is proposed which is able to account for all of these traits. The likely origin of the defect consists of a SiC in close proximity to a SF-type defect. *Ab initio* calculations are performed to support the validity of this model. The realization of bright stable electrically driven single-photon emission in SiC, in addition to the demonstration of pulsed excitation of the fully polarized single photons, is an important step towards on-demand single photons for applications in quantum information processing, quantum cryptography and single-photon metrology.

Methods

Device fabrication. The devices were fabricated on epilayers grown on 4H–SiC substrates by chemical vapour deposition purchased from CREE. The thickness and doping concentration was 4.9 μm and 4×10^{15} cm^{-3}, respectively. Multiple energy Al implantation was performed into the epilayers while the sample was held at 800 °C to form the p^+ regions. The implantation energies were chosen so as to form a nearly uniform dopant concentration depth profile over a 150 nm range. Following implantation an anneal of 1,800 °C for 10 min in an Ar ambient was used to activate the implanted dopants, repair the implantation damage and also form the single-photon emitters. The carbon film was removed using a dry oxidation process at 800 °C following the method described in ref. 18.

A 1,100 °C pyrogenic oxidation (H_2:O_2 = 1:1) was then performed to grow a field oxide. This had the effect of bringing the SiC surface closer to the peak in the implanted dopant profile to allow the formation of high-quality Ohmic contacts. This oxidation step was also found to reduce the PL background. The contacts were formed by Al deposition and subsequent sintering at 850 °C for 5 min. A back contact was formed by Al deposition without sintering. Full electrical characterization was then performed using current–voltage and capacitance–voltage measurements. The PL experiments were performed with HPSI 4H–SiC from CREE. Selected samples were irradiated with 2 MeV electrons to a fluence of 1×10^{17} cm^{-2} while the sample temperature was kept below 80 °C in a N_2 ambient to create a homogeneous defect density. Both as-grown and irradiated samples were annealed at 1,650 °C for 10 min in Ar. Carbonization of the surface and a subsequent 1,100 °C oxidation of these samples were also investigated. The HPSI wafer was on-axis and the n-type epi-layer used in the diode was 4° off-axis.

Confocal fluorescence microscopy. A custom confocal system consisting of a Hanbury Brown and Twiss interferometer and single-photon-sensitive avalanche photodiodes was used to measure the time correlation of the fabricated single-photon emitters. Photon counting and correlation were carried out using a time-correlated single-photon-counting module (PicoHarp 300, PicoQuant GmbH). The devices were driven in forward bias and the EL collected with a ×100 infinity-corrected air objective lens with a NA of 0.95. The luminescence was collected through a 50 μm multimode fibre pinhole. Optical excitation was achieved with a 532 nm continuous-wave laser directed through the objective via a dichroic mirror. Spectra were collected with a spectrometer (Princeton Instruments Acton 2300i, Acton) with a Peltier-cooled CCD. Samples were mounted on a piezoelectric XYZ stage allowing 100 × 100 μm^2 scans. The laser line or, during EL experiments, the D_1 line was spectrally removed with a 560-nm long-pass filter. The single-photon measurements were performed at room temperature.

The histogram $H(\tau)$ obtained from time correlation measurements was normalized by $H_{norm}(\tau) = H(\tau)/(N_1 N_2 \delta t T)$ and, when required, corrected for the underlying uncorrelated background to obtain the corrected autocorrelation function, $g^{(2)}(\tau) = (H_{norm}(\tau) - (1-\rho^2))/\rho^2$ (ref. 23). Here, N_1 and N_2 are the detector count rates, δt the bin width, T the acquisition time and ρ the signal-to-background ratio.

For low-temperature measurements the sample was mounted in a nitrogen cooled cryostat (Linkam THMS600). Instead of a XYZ stage, a scanning mirror was used. The emission was excited and collected through a cover slip corrected ×40 air objective with a NA of 0.6. Optical excitation was driven by either a 532 nm or a 633 nm continuous-wave laser. The 633 nm laser was required to excite emitters with ZPL positions at higher wavelengths.

Modelling. The atomistic simulations were carried out using density functional plane wave supercell calculations. Our working model is the isolated silicon antisite defect (Si_C) in bulk and near or inside regularly ordered SFs, that is, polytype inclusions. We studied the Si_C defect at the hexagonal site of 4H–SiC in detail. We

do not find qualitative differences in the ground state properties of Si_C defect at the cubic or hexagonal sites. The Si_C defect has a C_{3v} symmetry. To eliminate the finite size effect of the simulated cell we applied a very large supercell consisting of 1,536 atoms of bulk 4H–SiC in which to embed the defect. We applied Γ-point sampling of the Brillouin-zone that is sufficient to provide convergent charge density and enabled us to study the degeneracy of the defect levels. We applied the Perdew–Burke–Ernzerhof (PBE) semilocal density functional theory (DFT)[29] in most of the calculations. The PBE functional introduces a bandgap error of about 0.9 eV in SiC. However, we checked the ground-state properties of the Si_C defect in a 576-atom supercell with HSE06 hybrid DFT[30] which is able to reproduce the experimental bandgap of 4H–SiC ($\approx$3.2 eV) and defect levels in the fundamental bandgap[31,32]. By comparing the PBE and HSE06 results we found that a rigid scissor correction on the conduction band edge in the PBE calculation provided a very good description of the single particle levels of the defect state and conduction band edge with respect to the calculated valence band edge. The value of this scissor correction for the ZPL peak of Si_C defect is 0.81 eV.

The ZPL energies were calculated with the constraint DFT method where the excited state is created by promoting a single electron from the occupied state to the empty state[33]. We also calculated *ab initio* the ZPL peak of the Si_C defect near one cubic SF in 4H–SiC that may be considered as a half unit of a 6H polytype inclusion. As a consequence, the bandgap of the system is reduced by 0.23 eV due to the new conduction bands introduced by the SF acting as a quantum well for electrons. We used a 3,016-atom supercell for this study which involves five 4H–SiC unit cells and two extra cubic bilayers (SFs) along the *c*-direction of the lattice. Two SFs are needed because of the periodic boundary condition along the *c* axis. These two SFs were placed as far away from each other as possible ($\sim$2.5 nm). We placed the Si_C defect at a hexagonal site nearest to the SF and then three and five bilayers apart. We found that the calculated ZPL peaks of these defects approach the ZPL peak of Si_C defect in perfect 4H–SiC as the Si_C defects lie farther from the SF. The *ab initio* results indicate that the bulk ZPL wavelength is obtained when the Si_C defect resides at least $\sim$ 1 nm from the SF. The same phenomena is expected to arise for larger polytype inclusions such as 3C inclusions that should contain a minimum of three consecutive cubic bilayers. However, these structures are not computationally feasible at the *ab initio* level.

For realistically large 3C polytype inclusions in 4H–SiC we applied a simplified quasi-one-dimensional model which adequately describes the electronic structure of the defect either near or inside the 3C polytype inclusions (see ref. 34 for technical and other details). The code used to calculate the ZPL peaks of polytype inclusions[34] was modified so that the hole is localized at the defect site whereas the electron is attracted into the lowest-energy state of the triangular potential well in the SF if the defect is in its neighbourhood. The localization of the hole is achieved by adding an attractive potential for the hole. This attractive potential was set to reproduce the experimental ZPL peak of the Si_C defect in bulk 4H–SiC and then the same attractive potential was applied in the polytype inclusion model. This methodology was justified from *ab initio* calculations on the Si_C defect in bulk 4H–SiC and near to a SF and showed that the hole is a deep defect state localized around the defect where its level lies at about 0.2 eV above the valence band edge.

References

1. Nakamura, D. *et al.* Ultrahigh-quality silicon carbide single crystals. *Nature* **430,** 1009–1012 (2004).
2. Yamada, S., Song, B.-S., Asano, T. & Noda, S. Silicon carbide-based photonic crystal nanocavities for ultra-broadband operation from infrared to visible wavelengths. *Appl. Phys. Lett.* **99,** 201102 (2011).
3. Laube, M. *et al.* Electrical activation of high concentrations of n^+ and p^+ ions implanted into 4H–SiC. *J. Appl. Phys.* **92,** 549 (2002).
4. Castelletto, S. *et al.* A silicon carbide room-temperature single-photon source. *Nat. Mater.* **13,** 151–156 (2014).
5. Widmann, M. *et al.* Coherent control of single spins in silicon carbide at room temperature. *Nat. Mater.* **14,** 164–168 (2015).
6. Fuchs, F. *et al.* Engineering near-infrared single-photon emitters with optically active spins in ultrapure silicon carbide. *Nat. Commun.* http://dx.doi.org/10.1038/ncomms8578 (2015).
7. Christle, D. J. *et al.* Isolated electron spins in silicon carbide with millisecond coherence times. *Nat. Mater.* **14,** 160–163 (2014).
8. Castelletto, S. *et al.* Room temperature quantum emission from cubic silicon carbide nanoparticles. *ACS Nano* **8,** 7938–7947 (2014).
9. Morfa, A. J. *et al.* Single-photon emission and quantum characterization of zinc oxide defects. *Nano Lett.* **12,** 949–954 (2012).
10. Yuan, A. *et al.* Electrically driven single-photon source. *Science* **295,** 102–105 (2002).
11. Heindel, T. *et al.* Electrically driven quantum dot-micropillar single photon source with 34% overall efficiency. *Appl. Phys. Lett.* **96,** 011107 (2010).
12. Ward, M. B. *et al.* Electrically driven telecommunication wavelength single-photon source. *Appl. Phys. Lett.* **90,** 063512 (2007).
13. Hargart, F. *et al.* Electrically driven quantum dot single-photon source at 2 GHz excitation repetition rate with ultra-low emission time jitter. *Appl. Phys. Lett.* **102,** 011126 (2013).
14. Bennett, A. J. *et al.* Microcavity single-photon-emitting diode. *Appl. Phys. Lett.* **86,** 181102 (2005).
15. Lohrmann, A. *et al.* Diamond based light-emitting diode for visible single-photon emission at room temperature. *Appl. Phys. Lett.* **99,** 251106 (2011).
16. Mizuochi, N. *et al.* Electrically driven single-photon source at room temperature in diamond. *Nat. Photon.* **6,** 299 (2012).
17. Santori, C., Fattal, D. & Yamamoto, Y. *Single-Photon Devices and Applications* (John Wiley & Sons, 2010).
18. Negoro, Y., Katsumoto, K., Kimoto, T. & Matsunami, H. Electronic behaviors of high-dose phosphorus-ion implanted 4H–SiC (0001). *J. Appl. Phys.* **96,** 224 (2004).
19. Fuchs, F. *et al.* Silicon carbide light-emitting diode as a prospective room temperature source for single photons. *Sci. Rep.* **3,** 1637 (2013).
20. Berhane, A. M. *et al.* Electrical excitation of silicon-vacancy centers in single crystal diamond. *Appl. Phys. Lett.* **106,** 171102 (2015).
21. Gali, A. *et al.* Correlation between the antisite pair and the D_I center in SiC. *Phys. Rev. B* **67,** 155203 (2003).
22. Eberlein, T. A. G., Jones, R., Öberg, S. & Briddon, P. R. Density functional theory calculation of the DI optical center in SiC. *Phys. Rev. B* **74,** 144106 (2006).
23. Beveratos, A. *et al.* Room temperature stable single-photon source. *Eur. Phys. J. D* **18,** 191–196 (2002).
24. Kolesov, R. *et al.* Optical detection of a single rare-earth ion in a crystal. *Nat. Commun.* **3,** 1029 (2012).
25. Kitson, S. C., Jonsson, P., Rarity, J. G. & Tapster, P. R. Intensity fluctuation spectroscopy of small numbers of dye molecules in a microcavity. *Phys. Rev. A* **58,** 620 (1998).
26. Brillson, L. J., Tumakha, S., Okojie, R. S., Zhang, M. & Pirouz, P. Electron-excited luminescence of SiC surfaces and interfaces. *J. Phys. Condens. Matter* **16,** S1733 (2004).
27. Iwata, H., Lindefelt, U., Öberg, S. & Briddon, P. R. A new type of quantum wells: stacking faults in silicon carbide. *Microelectron. J.* **34,** 371–374 (2003).
28. Egilsson, T., Bergman, J. P., Ivanov, I. G., Henry, A. & Janzén, E. Properties of the D_I bound exciton in 4H–SiC. *Phys. Rev. B* **59,** 1956 (1999).
29. Perdew, J. P., Burke, K. & Ernzerhof, M. Generalized gradient approximation made simple. *Phys. Rev. Lett.* **77,** 3865 (1996).
30. Izmaylov, A. F., Krukau, A. V., Vydrov, O. A. & Scuseria, G. E. Influence of the exchange screening parameter on the performance of screened hybrid functionals. *J. Chem. Phys.* **125,** 224106 (2006).
31. Deák, P., Aradi, B., Frauenheim, T., Janzén, E. & Gali, A. Accurate defect levels obtained from the HSE06 range-separated hybrid functional. *Phys. Rev. B* **81,** 153203 (2010).
32. Ivády, V., Gällström, A., Son, N.-T., Janzén, E. & Gali, A. Asymmetric split-vacancy defects in SiC polytypes: A combined theoretical and electron spin resonance study. *Phys. Rev. Lett.* **107,** 195501 (2011).
33. Gali, A., Janzén, E., Deák, P., Kresse, G. & Kaxiras, E. Theory of spin-conserving excitation of the NV^- center in diamond. *Phys. Rev. Lett.* **103,** 186404 (2009).
34. Castelletto, S. *et al.* Quantum-confined single photon emission at room temperature from SiC tetrapods. *Nanoscale* **6,** 10027–10032 (2014).
35. Davydov, S. Yu., Lebedev, A. A. & Posrednik, O. V. Estimates of the exciton transition energy in NH/3C/NH (N = 2, 4, 6, 8) heterostructures based on silicon carbide polytypes. *Semiconductors* **40,** 549–553 (2006).

Acknowledgements

B.C.J. acknowledges the Australian Research Council Center for Quantum Computation and Communication Technology (CE110001027) and the Dyason Fellowship for financial support. T.O. acknowledges the Ministry of Education, Science, Sports and Culture, Grant-in-Aid (B) 26286047. A.G. acknowledges the Lendület program of the Hungarian Academy of Sciences and the Hungarian OTKA grant nos K101819 and K106114.

Author contributions

A.L. and B.C.J. designed and performed the experiment, did the data analysis and prepared the manuscript. A.G. and Z.B. performed the *ab initio* calculations and related analysis. N.I. and T.O. fabricated the devices. All authors discussed the results and contributed to the manuscript.

Additional information

Supplementary Information accompanies this paper at http://www.nature.com/naturecommunications

Competing financial interests: The authors declare no competing financial interests.

Reprints and permission information is available online at http://npg.nature.com/reprintsandpermissions/

How to cite this article: Lohrmann, A. *et al.* Single-photon emitting diode in silicon carbide. *Nat. Commun.* 6:7783 doi: 10.1038/ncomms8783 (2015).